ADVANCED MATERIALS

Supporting Information

for *Adv. Mater.,* DOI: 10.1002/adma.201501058

Toward 3D Printing of Pure Metals by Laser-Induced Forward Transfer

Claas Willem Visser, Ralph Pohl,* Chao Sun, Gert-Willem Römer, Bert Huis in 't Veld, and Detlef Lohse*

Supplementary material of: Towards 3D printing of pure-metal electronics by laser-induced forward transfer

C.W. Visser, R. Pohl, C. Sun, G.R.B.E. Römer, A.J. Huis in 't Veld, D. Lohse

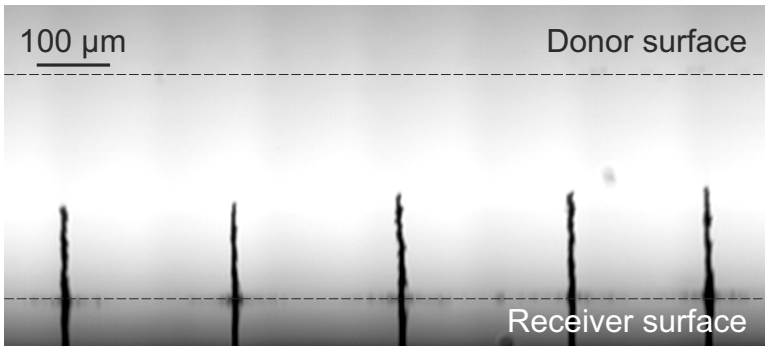

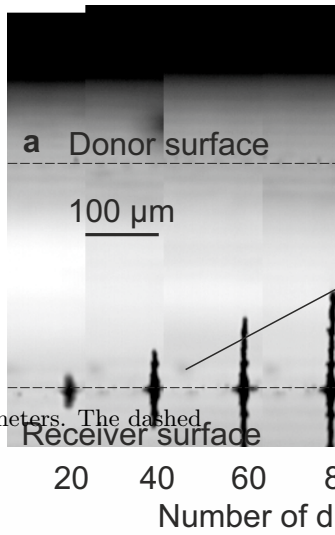

Supplementary Figure 1. Deposition of five pillars on the same receiver while using the same process parameters. The dashed lines indicate the (reflective) donor and receiver surfaces.

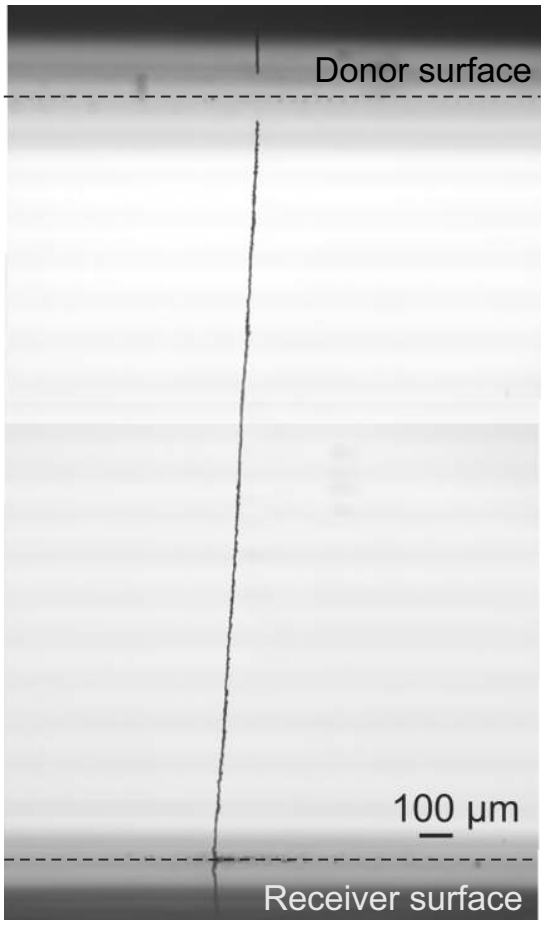

Supplementary Figure 2. Gold pillar with a height of 2.1 mm, illustrating the potential for fabrication of free-standing structures.

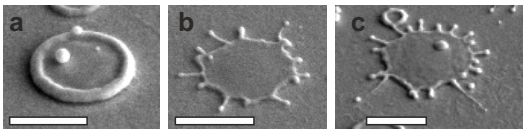

Supplementary Figure 3. Detailed view of solidified drops in the (a) rim and (b,c) splash deposition regimes. The splash images correspond to the splash threshold, since the ejected drops at the edge of the main drop are still partly connected by thin threads. The scale bars indicate 1 µm; the images were taken for impact in the jet ejection regime [1] at $F = 8 \cdot 10^3$ Jm^{-2}.

SUPPLEMENTARY NOTE 1: DETAILED METHODS

A. LIFT ejection

The experimental setup is shown in figure 1 of the main text. The main laser is an Yb:YAG laser with a pulse duration $\tau_L = 6.7$ ps, a wavelength of 515 nm, a Gaussian beam profile with quality factor $M^2 < 1.3$, and maximum peak fluence error of 200 J m^{-2}. The beam is focused to a diameter ($1/e^2$) of $D_L = 17$ µm at the carrier-donor interface, using an f-theta scan-lens with a 100 mm focal length. The fluences in this article are the peak fluences on the laser symmetry axis. A $d = 200 \pm 20$ nm copper donor layer is sputtered onto a 1 mm thick glass carrier. A clean glass microscope slide coated with a 100 nm copper film is used as a receiver substrate.

B. Real-time visualization

Images are recorded using a microscope with a 50×long-distance objective and a dual-shot CCD camera (PCO Sensicam qe, PCO, Germany). A dual-cavity Nd:YAG laser (pulse duration 6 ns) is used for bright-field flash illumination. To prevent coherence, a high-efficiency diffuser is placed in between the laser and the camera. The illumination laser and the camera are synchronized to the main laser by a BNC 575 pulse-delay generator, which in turn is triggered by the output of a photodiode connected to the LIFT laser beam path. This provides two flash-illuminated frames of each ejection with a minimum frame-to-frame time of 350 ns, which were contrast-enhanced for optimal visualization.

C. Pillar cutting and visualization

The pillars were analyzed with a FEI Dualbeam Nova600 Nanolab using a focused ion beam for cross-sectioning and a scanning electron microscope for imaging. The cross-sectioning cut was made with an ion beam of 23nm in diameter at full width half maximum (setting: 30kV, 90pA) to prevent damaging the internal structure. However the shadowing effect, the so called curtain effect, cannot be prevented. The images are made by the SEM within the FEI Dualbeam Nova 600 Nanolab.

D. AFM pillar deflection measurements

To determine the pillar radius r, atomic force microscopy measurements were performed providing the deflection δ of a beam as a function of the force F_{AFM}, as shown in figure 4b. After each measurement, the pillar was relaxed to its original position to ensure no plastic deformation of the pillar. The deflection is plotted as a function of the force in supplementary figure 4. The deflection increases linearly with the force, as expected for elastic deformation, and the lines indicate fits to obtain the pillar thickness. Now, the thickness is obtained using

$$\delta = \frac{FL^3}{3EI}, \text{ with } I = \frac{\pi}{4} r^4, \qquad \text{(Supplementary Equation 1)}$$

with L and I being the probe distance and the moment of inertia, respectively. Since the microstructure is unknown, a (bulk) young modulus E of 117 GPa is assumed. Finally, to cross-check this approach and to assess whether the pillars are homogeneous in thickness, the shape of the deflected pillar is compared to the theoretical solution for a bent beam of homogeneous thickness according to equation (Supplementary Equation 1). As shown in figure 4a, good agreement is observed, which confirms the homogeniety of the pillars.

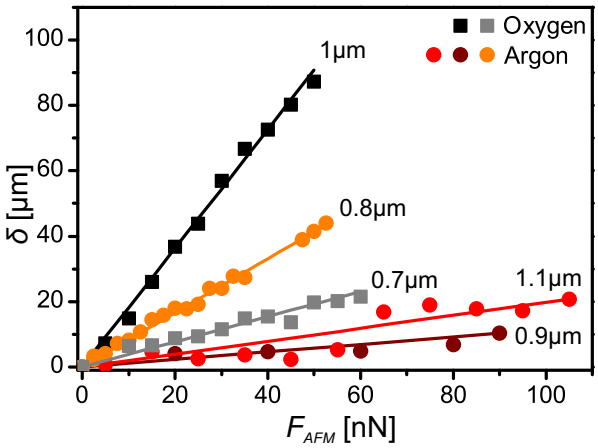

Supplementary Figure 4. Atomic force microscopy measurements of the deflection of the pillar tip as a function of the force applied. The linear dependency corresponds to elastic deformation of a beam with a homogeneous thickness; the lines are different since the deflection δ is measured at a different pillar height for each pillar. The lines are fits used to determine the radius of each pillar, as indicated next to each line. The square markers indicate pillars processed in air, the round markers correspond to pillars processed in argon, and different colors indicate different pillars. Here we measure pillar radii in the range $r = 0.9 \pm 0.15$ μm, as indicated next to the pillars. This radius is used as an input parameter for the electrical conductivity measurements.

E. Resistivity measurements

The electrical properties of the pillars are measured by connecting electrodes to the donor- and receiver substrates, and gently pressing the donor onto the tip of the pillar. In this way, the circuit is closed and the resistance is measured. The resistance consists of the contact resistance R_c and the resistance of the pillar itself. By measuring this resistance during the deposition process, i.e. for pillars of increasing length, increasing values of the resistance are obtained. A linear fit of the $R(h)$ curve provides the (constant) contact resistance R_c as its offset, and the slope provides the pillar resistance per unit length. The resisitivity of the conducting lines was measured using 4 point probe-measurements (to exclude the influence of the contact resistance), by measuring the resistance between conductive pads as shown in figure 4h.

F. Drop impact simulations

Simulations were done using the open-source flow solver Gerris [2], which numerically solves the incompressible Navier-Stokes equation on a non-uniform flow-adaptive grid. The size of the (squared) simulation domain is 3 drop diameters, with outflow boundary conditions on the top and left edge, no-flow conditions on the bottom edge and symmetry conditions on the right edge (which represent the z-axis along which the drop approaches the surface). The simulation shown in figure 5 corresponds to drop impact for We = 150 and Re = 696. A further description and an extensive validation against experiments are provided in ref. [3].

SUPPLEMENTARY NOTE 2: TIME SCALE CALCULATIONS

Time scale definitions: The time scales of drop spreading (τ_I) and retraction (τ_R) will now be discussed for an impacting drop with diameter D_0 impacting at velocity V_0 (see figure 5c). We consider inertial impact, i.e. Re $\gg 1$ and We $\gg 1$. Here, $\mathrm{Re} = \rho D_0 V_0/\nu$ is the Reynolds number, which denotes the ratio between inertial energy to viscous dissipation, ρ is the drop's density, and the temperature-dependent viscosity $\nu(T)$ is calculated according to ref. [4]. $\mathrm{We} = \rho D_0 V_0^2/\sigma$ is the Weber number, representing the ratio between inertial energy and surface energy with σ the surface tension. The input variables D_0, D_{max}, and V_0 are calculating as follows. To obtain the drop diameter D_0, the volume ejected from the donor layer is obtained by measuring the crater size and depth, and assuming a spherical drop shape. The drop impact velocity V_0can be assumed to be equal to the ejection velocity, for which we recently derived and validated a model [1].

Upon impact, the drop spreads out over the surface and flattens until a maximal spreading diameter D_{max} is

reached (see figure 5e). The moment at which D_{max} is reached corresponds to the inertial time scale:

$$\tau_I = 3D_0/V_0, \qquad \text{(Supplementary Equation 2)}$$

in which the prefactor of 3 is based on our previous experiments and simulations [3]. The maximal spreading diameter of the drop is estimated using the model of Roisman [5]:

$$\frac{D_{max}}{D_0} = 0.87\mathrm{Re}^{1/5} - 0.4\mathrm{Re}^{2/5}\mathrm{We}^{-1/2} \qquad \text{(Supplementary Equation 3)}$$

This model includes both the inertial spreading dynamics and the rim formation, and is known to well describe experimental data for We $\gtrsim 10$ [3].

Next, surface tension has a profound influence on the retraction dynamics of the drop. In particular, a rim develops at the edge of the drop (see figure 5e), which keeps growing also after the maximum spreading radius is reached and thus contracts the drop. Eventually, for non-wetting impact surfaces, the drop contracts back into a sphere, which can even bounce away from the surface. This contraction occurs on a capillary time scale [6]

$$\tau_R = \frac{D_0}{D_{max}}\sqrt{\frac{2\rho D_0^3}{3\sigma}}. \qquad \text{(Supplementary Equation 4)}$$

Finally, we estimate the time for the drop to solidify, by assuming that the drop solidified after its melting enthalpy Q_{melt} is transferred to the substrate. We estimate $Q_{melt} = \pi D_{max}^2 h\Delta H/4$, with h the height of the drop when spread-out, $\pi D_{max}^2 h/4$, the drop volume, and ΔH the enthalpy of fusion per unit volume. The substrate is modeled as a semi-infinite solid, for which the time-integrated heat transfer until time t is given as $Q(t) = 0.5\pi D_0^2 k\Delta T\sqrt{t/(\pi\alpha_{th})}$, with α_{th} the thermal diffusivity, k the thermal conductivity, and ΔT the (assumed to be constant) temperature difference between the drop and the substrate [7]. The solidification time scale is then obtained by solving the equation $Q_{melt} = Q(\tau_{th})$, yielding:

$$\tau_{th} = \alpha_{th}\pi\left(\frac{h\Delta H}{2k\Delta T}\right)^2. \qquad \text{(Supplementary Equation 5)}$$

As we expect that heat diffusion is limited primarily by the substrate properties, α_{th} and k are chosen for the substrate.

Unfortunately, theoretical optimization of the solidification time scale is still out of reach, since unknown parameters (the surface melting and vaporization kinetics, the surface and drop's oxide layer thickness, and the cooling and oxidation during the time of flight) and insufficiently understood physical mechanisms regarding drop solidification (the influence of the substrate temperature, the surrounding gas pressure, and surface roughness) are required [8, 9]. Still, equation (Supplementary Equation 5) may support empirical optimization of the receiver substrate. In particular, changing the surface conductivity will have a strong (linear) effect on the solidification time scale, and this parameter can be easily varied over several orders of magnitude.

[1] R. Pohl, C. W. Visser, G.-W. Römer, D. Lohse, C. Sun, B. Huis in t Veld. *Physical Review Applied* **2015**, *3*, 2 024001.
[2] S. Popinet. *Journal of Computational Physics* **2009**, *228*, 16 5838.
[3] C. W. Visser, P. E. Frommhold, S. Wildeman, R. Mettin, D. Lohse, C. Sun. *Soft Matter* **2015**, *11* 1708.
[4] G. Kaptay. *Zeitschrift für Metallkunde* **2005**, *7* 1.
[5] I. V. Roisman. *Physics of Fluids* **2009**, *21*, 5 052104.
[6] D. Bartolo, C. Josserand, D. Bonn. *Journal of Fluid Mechanics* **2005**, *545* 329.
[7] A. Bejan. *Heat Transfer*. John Wiley & Sons, INC., Durham, NC, USA, 1 edition, **1993**.
[8] P. Fauchais, M. Fukumoto, A. Vardelle, M. Vardelle. *Journal of Thermal Spray Technology* **2004**, *13*, 3 337.
[9] S. Chandra, P. Fauchais. *Journal of Thermal Spray Technology* **2009**, *18*, 2 148.